Microstructural and Tribo-mechanical Properties of Arc-Sprayed CoCr-Based Coatings

L. Hagen[1] · M. Paulus[2] · W. Tillmann[1]

Abstract Due to their superior wear and oxidation resistance, Stellite[TM] coatings are widely used in industrial applications, where the coatings are exposed to high temperature. Common processes for applying Stellite[TM] coatings include the high-velocity oxy-fuel spraying, laser cladding, and plasma transferred arc welding. Although Stellite[TM] welding consumables or similar welding consumables in the form of cored wires (CoCr base without industrial property rights) are commercially available, there are hardly any studies on arc-sprayed Stellite[TM] coatings available in the literature. In this study, the microstructural characteristics of arc-sprayed deposits were investigated, which were produced using a CoCr-based cored wire with addition of 4.5 wt.% tungsten. The produced deposits were examined in its as-sprayed state as well as after exposed to elevated temperatures. The microstructure was scrutinized by means of electron microscopy, energy-dispersive x-ray spectroscopy, as well as x-ray diffraction analyses using synchrotron radiation. Tribo-mechanical tests were conducted in order to assess the performance of the arc-sprayed coating. The findings were discussed and compared to those obtained from conventional CoCr-based coatings. It was found that the arc-sprayed CoCr-based coating is predominantly composed of Co-rich, Cr-rich lamellae or lamellae comprising a Co(Cr)-rich solid solution interspersed with various oxides between the individual lamellae. Solid solution

✉ L. Hagen
leif.hagen@tu-dortmund.de

1 Institute of Materials Engineering, TU Dortmund University, Dortmund, Germany

2 Fakultät Physik/DELTA, TU Dortmund University, Dortmund, Germany

hardening serves as dominant strengthening mechanism, while precipitation hardening effects are hardly evident. With regard to the oxidation behaviour, the as-sprayed coating mainly contains $CoCr_2O_4$ as well as traces of Co_3O_4. For heating above 550 °C, coating surface additionally consists of Fe_2O_3 and Co_3O_4. In dry sliding experiments, the arc-sprayed CoCr-based coating shows a decreased wear resistance compared to CoCr-based coatings processed by HVOF and PTA, whereas the coefficient of friction (COF) sliding against alumina was similar to the COF observed for the HVOF-sprayed CoCr-based coating, but lower than the COF obtained for the CoCr-based hardfacing alloy deposited by PTA.

Introduction

Stellite[TM] summarizes a group of hardfacing alloys based on the Co-Cr system with minor additions of W, Mo, V, Nb, Ta, Ni, B and C. The hardness of such coatings is mainly determined by the amount of the carbide forming agents, e.g. Cr, W, Mo, and C content. In contrast, the toughness is mainly provided by the Co content. The Co phase occurs in two allotropic modifications, i.e. face-centred cubic (fcc) and hexagonal close packed (hcp) lattice structure (Ref 1). The occurrence of the two phases depends on the temperature and pressure and is therefore dependent on production. For common CoCr-based hardfacing alloys, the increase in strength is caused by the addition of Cr as alloying element which leads to the formation of M_7C_3 and $M_{23}C_6$ (where M = metal) hard phases (Ref 2, 3). Other alloying elements such as Mo and W

increase the strength due to the formation of MC, M_6C, or $M_{12}C$-type hard phases as well as intermetallic phases such as $Co_3(Mo, W)$ (Ref 3-6). The carbide hard phases are predominantly present as precipitates in a Co-rich solid solution matrix. The microstructural characteristics of Stellite[TM] coatings, such as the size of carbide precipitates, their distribution and volume fraction, as well as the formation of dendritic structures, largely depend on the deposition process (i.e. the process control, and thus the solidification kinetics and cooling processes). Common methods for applying Stellite[TM] coatings include the high-velocity oxy-fuel (HVOF) spraying (Ref 6-10), laser cladding (Ref 8, 10, 11) and plasma transferred arc welding (PTA) (Ref 3, 5, 12). For some of these processes, the deposition of Stellite[TM] coatings to steel substrates goes along with the dilution from the steel substrate. Various studies (Ref 10-12) clarified that the level of dilution depends substantially on the deposition process (i.e. a dilution can be precluded even by using HVOF spraying). As a result, the mechanical properties can vary distinctly along the coating thickness close to the coating–substrate interface (Ref 10, 13). Among thermally sprayed hard coatings (e.g. WC-, Cr_3C_2-, or Co-based coatings), Stellite[TM] coatings show a comparatively good cavitation-erosion (Ref 14, 15), oxidation and corrosion resistance (Ref 16). Besides remarkable erosive (Ref 15) and abrasive wear resistance (Ref 17), Stellite[TM] coatings provide an outstanding wear resistance against sliding (Ref 6), as well as an excellent metal-to-metal friction behaviour with a simultaneous low tendency to galling (Ref 18). The superior wear resistance against sliding at ambient conditions is based on two effects: (i) the formation of carbide precipitates dispersed in the Co-based solid solution matrix, and (ii) the ability of the Co-based matrix to undergo plastic deformation. The latter can be attributed to strain-induced phase transformation processes from the fcc to the hcp structure, due to a low stacking fault energy, whereby the Co basal plane is aligned parallel to the sliding direction (Ref 19-21). At elevated temperatures, the superior sliding wear resistance and friction behaviour can be assigned to tribo-oxidation phenomena (Ref 22, 23). Studies describing the different mechanisms for the tribological behaviour for common Stellite[TM] coatings are summarized in (Ref 6).

Although Stellite[TM] welding consumables or other CoCr-based consumables (without proprietary rights) are commercially available (Ref 24, 25), only few studies of arc-sprayed Stellite[TM]-based coatings are available in the literature. For instance, Varavallo et al. (Ref 26) investigated the adhesion of an arc-sprayed Stellite[TM] 6 coating to steel substrates. Detailed examinations on the microstructural characteristics (e.g. phase composition) or coating performance in mechanical-technologically tests were not discussed by the authors or elsewhere in the literature. The absence of such studies currently does not allow a comparison between the coating properties of conventional (HVOF, PTA, laser cladding) CoCr-based coatings (i.e. Stellite[TM]) and arc-sprayed CoCr-based coatings.

Arc spraying is a well-established process for the fabrication of wear and corrosion protection coatings (Ref 27). Among thermal spraying, the main advantages of arc spraying are comparatively low acquisition and operating costs, simplified handling (including transportability), and extremely high energy efficiency coupled with high deposition rates during spraying (Ref 28). Compared to other joining techniques (e.g. laser cladding, PTA or other welding processes), a dilution from the substrate material can be precluded due to the inherent process characteristics (Ref 29). The splashing and overlapping of many individual spray particles results in the formation of a lamellar microstructure that depend primarily on the spray particle conditions at the moment of impact onto the substrate (Ref 30-34). The formation of spray particles (i.e. droplet formation) depends largely on the melting behaviour of the electrode tips and the prevailing flow regimes of the atomizing gas used (Ref 34-37). Hence, the atomization of the molten electrode tips (primary atomization) is determined by the aerodynamically driven disintegration, magnetofluiddynamic processes and material-specific properties of the melt (Ref 28, 38). For the use of compressed air as the atomization gas, arc-sprayed deposits are usually interstratified with a certain amount of oxides (Ref 31, 39, 40). Furthermore, with regard to the electrode phenomena, some constituents of the feedstock are heated above their melting point. Besides melting losses, the high temperatures may consequently lead to undesirable phase transformation processes (Ref 41, 42). The phase transformation processes and reaction kinetics depend on the environmental conditions (atmospheric, inert) (Ref 43) and thermodynamic aspects (Ref 38).

In this study, a first attempt has been made to analyse an arc-sprayed CoCr-based coating with regard to the resulting microstructural and tribo-mechanical properties. The produced deposits were examined in its as-sprayed state as well as after exposed to elevated temperatures. Mechanical properties such as microhardness and fracture toughness were investigated by means of indentation techniques. Additionally, dry sliding experiments were conducted to evaluate the friction behaviour and wear resistance against sliding. The findings were discussed and compared to those obtained from conventional CoCr-based coatings, i.e. Stellite[TM] 6 processed by HVOF and PTA.

Experimental

Substrate Material and Feedstock

Round steel (AISI 1045) specimens with a diameter of 40 mm and a thickness of 4 mm were employed as substrates. The surfaces of the steel substrates were grit blasted with corundum (grit size: F14 according to the Federation of European Producers of Abrasives, FEPA, standard 42–1:2006) using a blasting air pressure of 0.4 MPa, a stand-off distance of 100 mm, and a blasting angle of 45°. Prior to the coating deposition, the samples were cleaned in an ultrasonic ethanol bath and preheated in a convection oven to a temperature of about 80 °C. Within this study, a CoCr-based cored wire Durolit 6 (Co-29.7Cr-5.24 W-2.64Fe-1.47Ni-1.42Si-1.23C-1.17Mn wt.%, DURUM Verschleissschutz, Germany) served as feedstock. The cored wire consists of an outer sheath (i.e. velum) made of Co, whereas the other constituents served as filling.

Coating Process

In order to conduct the spraying experiments, the Smart Arc 350 PPG spraying system (Oerlikon Metco, Switzerland) was utilized. The spray torch was equipped with a conventional front-end hardware (high-profile centering post, No. PPG5I976; air cap body (fine), No. PPG51416). For the coating deposition, the spray torch was mounted on a 6-axis robot (ABB IRB 4600 60/2.05, ABB, Switzerland). The spray parameter settings derived from a multi-criteria optimization using statistical design of experiments and Derringer's desirability function (Ref 44), as shown in (Ref 45) for a CoCr-based coating. Accordingly, compressed air at a pressure of 0.95 MPa was utilized as atomization gas. The voltage and current were, respectively, set to 29 V, and 200 A. The spraying experiments were conducted at a constant spray distance of 115 mm. The transverse speed at which the spray torch moved over the sample was kept constant at 200 mm/s, while the track pitch of the meander-shaped robot path was set to 5 mm. Two passes were executed in order to generate an adequate coating thickness.

Within this study, a PTA overlay (feedstock: DUR-MAT® S6 PTA, Co-29.0Cr-4.2 W-1.2Si-1.0C wt.%, DURUM Verschleissschutz, Germany) as well as a HVOF-sprayed coating (feedstock: Stellite®6, Co-28.7Cr-4.4 W-1.1C-1.0Ni-1.0Si-0.05Fe wt.%, Oerlikon Metco Coating Services, formerly Terolab Surface, Germany) were provided by the supplier and served as references.

Analytic Methods

In order to examine the coating microstructure, cross sections of coated samples were prepared by using diamond grinding discs and polishing cloths with a diamond suspension (steps: 9, 6, 3, and 1 μm). Cross sections were analysed by means of light microscopy using an optical microscope (model BX51M, Olympus, Japan). The porosity was determined via cross-section images based on grey scale analysis with the integrated software Axiovision AutoMess. Cross-section images were taken with a 500 × magnification. Ten different spots across the coating were taken into account. Cross-section analyses in a magnified view were conducted using a field emission scanning electron microscope (FE-SEM) model JSM-7001F (Jeol, Germany) equipped with secondary electrons and backscattered electrons detectors. The element distribution was afterwards determined by means of energy-dispersive x-ray spectroscopy (EDS). The EDS spectra were obtained by using an energy-dispersive x-ray detector (Oxford Instruments, United Kingdom) in conjunction with the FE-SEM. The data obtained were afterwards analysed using the EDS microanalysis software INCA (Oxford Instruments, United Kingdom). The phase composition of the arc-sprayed CoCr-based coating was examined through XRD at the beamline BL9 of the synchrotron light source DELTA (Dortmund, Germany) (Ref 46). The photon energy was set to 13 keV (wavelength $\lambda = 0.9537$ Å) and a PILATUS 100 k detector (DECTRIS, Switzerland) was used for photon detection. The beam size was set to 0.1 mm (height) × 1.0 mm (width) and the angle of incidence was 5°. The feedstock (i.e. the filling and velum of the cored wire) was measured in transmission geometry. The software MATCH! (Crystal Impact, Germany) in conjunction with a reference database (i.e. Crystallography Open Database) was used to identify the phase composition. In order to study the oxidation behaviour of the produced CoCr-based coatings, polished coated samples were annealed at different temperatures (350, 450, 550, 650 and 750 °C) utilizing a heat plate (type DHS 1100, Anton Paar, Austria). The heating was conducted at atmosphere with a heating rate of 15 K/min. The holding time at each temperature was set to 10 min. The oxide formation after temperature exposure was investigated by means of XRD at the beamline BL9 of the synchrotron light source DELTA using a photon energy of 27 keV (wavelength $\lambda = 0.4592$ Å). The beam size was set to 0.1×1.0 mm^2 (v x h) and the angle of incidence was 3°. The scattered intensity was measured using a MAR345 image plate detector (marXperts, Germany).

The arc-sprayed CoCr-based coating, hereinafter referred to as AS-S6, was further investigated with respect to the tribo-mechanical properties. The PTA overlay and

HVOF-sprayed coating, referred to as PTA-S6 and HVOF-S6, faced same tests and served as references. Prior to the tribo-mechanical testing, the coating surfaces were machined using a silicon carbide grinding disc (grit size: P4000 according to FEPA), and polished utilizing polishing cloths with diamond suspension (abrasive particle size: 3 and ¼ μm). Tribological tests were performed in accordance with ASTM G99-05 using a pin-on-disc apparatus (Anton Paar Group, Austria, formerly CSM Instruments, Switzerland) at room temperature and without lubricant supply. For the dry sliding experiments, an alumina ball with a diameter of 6 mm and a hardness of 2300 HV0.3 was used as counterbody. The velocity was kept constant at 40 cm/s, and the radius of the circular path was set to 10 mm. A sliding distance of 200 m, and a load of 5 N were applied. The coefficient of friction (COF) was determined via measurements of the tangential force and the applied normal force. To determine the volumetric material loss, the wear track at the tribological stressed surface was surveyed by means of 3D-profilometry (Infinite Focus, Alicona, Austria) at four different position taken three samples into account. Electron microscopy and EDS (as described previously) were conducted to investigate the tribological stressed surface with regard to the element distribution and wear mode. The hardness, H, and Young's modulus, E, inside the wear track and at the non-tribological stressed surface were ascertained by means of nanoindentation, modelled after the method demonstrated by Oliver and Pharr (Ref 47). A total amount of 49 indents were conducted utilizing the nanoindenter G200 (Agilent Technology, California). The indents were performed with a diamond Berkovich indenter in depth-controlled mode considering a penetration depth of 2 μm, which represents the maximum penetration depth in order to avoid size effects (i.e. of individual specific phases) as much as possible. To avoid a distortion of the mechanical testing results, the distance between the indents was set to be 50 μm. For calculating the Young's modulus, the Poisson's ratio was set to 0.3 and was kept constant for all sample types. As shown in (Ref 48, 49), the H/E ratio (i.e. plasticity index) and the H^3/E^2 ratio (i.e. an indication of the resistance to plastic deformation Ref 50) are significant factors governing sliding wear behaviour. For this purpose, the H/E and H^3/E^2 ratio were calculated from the data obtained. To minimize the risks of size effects corresponding to the microstructural heterogeneity, Vickers microhardness measurements were additionally carried out inside the wear track and at the non-tribological stressed surface using the M-400 microhardness tester (LECO, Michigan) with a load of 2.94 N. The diameter of the remaining indentation was measured with an optical microscope with integrated image analysis software (see above). The Vickers microhardness was determined by taking five indents into account. In addition to the Vickers microhardness tests, the fracture toughness K_{IC} was determined as described in (Ref 51) based on the model suggested by Niihara (Ref 52), examining indentation-induced Palmqvist cracks. The surface length of the Palmqvist cracks varies linearly with the indentation load, allowing the indentation tests to be performed at different loads. Thus, a higher indentation load was utilized for the samples PTA-S6 and HVOF-S6, in order to provoke cracks as far as possible, whereas the influence of the substrate and embedding resin should be avoided due to excessive loads at the same time. Accordingly, Vickers indentation tests were conducted with a load of 39.23 N for the sample AS-S6, as well as 98.07 N for the samples PTA-S6 and HVOF-S6 at the cross section using a DIA-TESTOR 7521 universal hardness tester (Wolpert, Germany).

The phase composition at the non-tribological stressed surface of the samples AS-S6, PTA-S6 and HVOF-S6 was examined via XRD at the beamline BL9 of the synchrotron light source DELTA using a photon energy of 13 keV and a PILATUS 100 k detector as described previously.

Results

Microstructure

Figure 1 shows the morphology of the arc-sprayed CoCr-based coating (sample AS-S6) in its as-sprayed state taken at the cross section. As shown by the scanning electron microscope (SEM) image, the produced coating exhibits a low porosity without distinct defects such as macropores or cracks. Image analysis at higher magnifications indicates an overall porosity less than 1% with only very few micropores.

Cross-section analysis at the coating–substrate interface demonstrates the absence of interfacial cracks, suggesting an adequate bonding to the steel substrate. EDS line scans at the coating–substrate interface show that the amount of Fe in the coating close to the coating–substrate interface does not exceed the amount of Fe as obtained from other regions of interest (i.e. in the vicinity), or that of the nominal amount provided by the feedstock (Fig. 2). Hence, the dilution of Fe originating from the steel substrate can be precluded.

With respect to the coating cross-section analysis, the backscattered electrons (BSE) image demonstrates that the coating is characterized by a lamellar microstructure, wherein the individual lamellae consists of a different chemical composition (see Fig. 1, magnified view). Quantitative EDS analysis at different spots of the representative coating microstructure reveals that the coating exhibits an average content of 52.88 wt.% of Co, 27.21
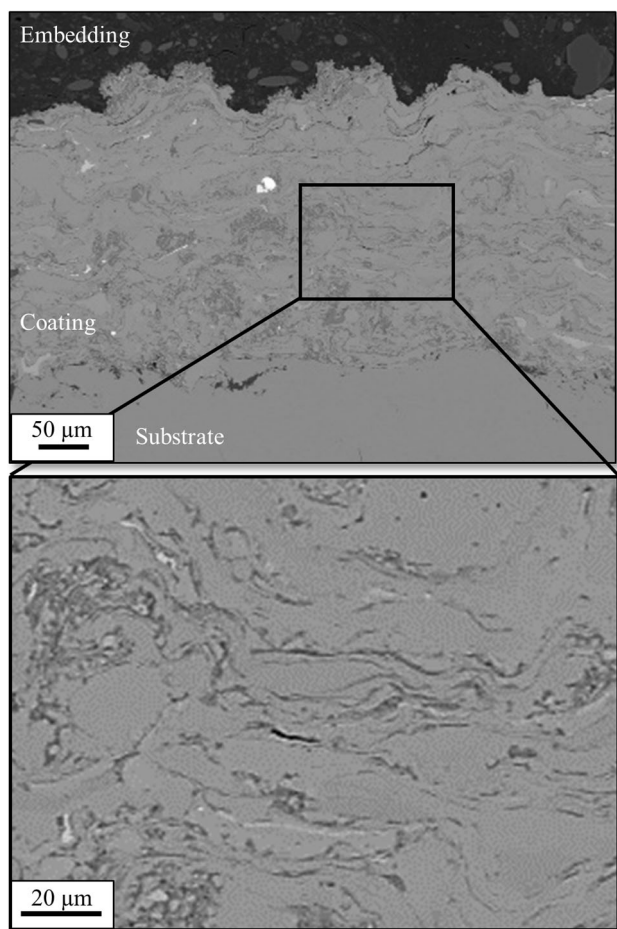
Fig. 1 SEM images showing the microstructure of the arc-sprayed CoCr-based coating
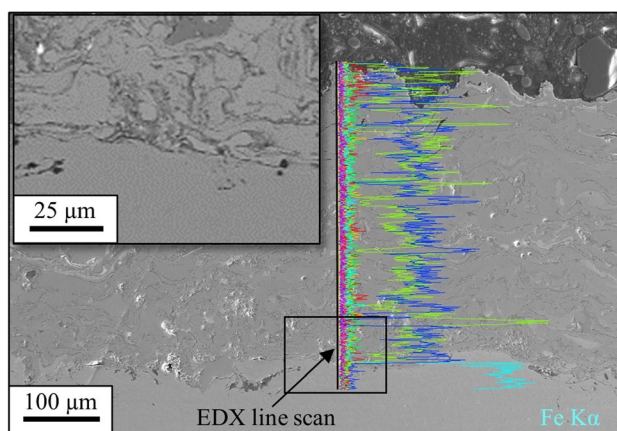

Fig. 2 SEM image showing the EDS line scan at the coating–substrate interface with its corresponding element distribution for Fe Kα

wt.% of Cr, 3.82 wt.% of W, 3.40 wt.% of Fe, 2.38 wt.% of Ni, and 1.71 wt.% of C, with both Si and Mn < 1 wt.%. In addition, the coating features an average content of 7.19 wt.% of O, suggesting the formation of oxides. Despite the

formation of oxides, the findings confirm that the composition of the samples mainly corresponds to the nominal composition of the feedstock. Slight deviations can be attributed to local microstructural heterogeneity, or element losses caused by the electrode phenomena during arc spraying. Figure 3 shows the BSE image of the coating microstructure and the corresponding EDS maps obtained from O Kα, Cr Kα, Co Kα, and W Lα at the cross section. For the region of interest, it can be seen that the coating consists of individual lamellae composed of Co-rich and Cr-rich phases or Co(Cr)-rich solid solutions. W-rich lamellae (bright phases) scatter randomly throughout the coating. Those W-rich lamellae are surrounded by a Co(Cr)-rich matrix (dark areas). Moreover, the EDS maps demonstrate the presence of Co-rich and Cr-rich oxides. It is found that the oxides are predominantly formed between individual lamellae, suggesting the occurrence of mixed oxides which in turn depend on the chemical composition of individual lamellae. Further electron microscopic investigations verify that W-rich phases are either present as lamellar shaped (splat-like shaped) phases or globular shaped phases embedded in the surrounding matrix (Fig. 4). EDS spot analysis (Fig. 4, spectrum 1 to 5) demonstrates that the W-rich phases predominantly consist of a solid solution of Co, Cr and W. As seen by the EDS line scans (Fig. 4, spot A versus spot B), the variation in brightness corresponds to varying Cr, Co and W contents. Although a precise determination of light elements by means of EDS is precluded, C and O were not omitted from the measurements. Accordingly, the data suggest the absence of tungsten carbides for the selected regions of interest, i.e. spots A and B.

XRD analysis reveals that the arc-sprayed CoCr-based coating (sample AS-S6) mainly consists of cubic and hexagonal Co, Cr and $CoCr_2$ (Fig. 5). M_xC_y-type (M = metal) carbides cannot be found within the experimental resolution. Whether this is due to a decomposition of the carbides or to the fact that the relative scattering strengths of the carbides are too low compared to Co and Cr cannot be determined by the experimental data. As opposed to that, the velum is composed of pure Co with fcc structure. The XRD pattern of the filling shows a rich spectrum of Bragg reflections, which can be assigned to Cr with body-centred cubic (bcc) structure, Cr_3C_2 and Si (to a lesser extent). The few remaining reflections cannot be clearly assigned due to their low intensity and number. Crystalline W was not detected within the experimental resolution.

With regard to the oxidation behaviour, it is found that the coating in its as-sprayed state (i.e. at room temperature) contains $CoCr_2O_4$ (or $CoFe_2O_4$), see Fig. 6. The small peak reflection at $2\theta = 10.77°$ indicates the presence of Co_3O_4 (or $Co_{2.74}O_4$, $Co_{2.62}O_4$). In addition, the XRD pattern suggests a slight amount of $NiFe_2O_4$ (or $Ni_{1.43}Fe_{1.7}O_4$), as

Fig. 3 SEM image showing the coating microstructure and corresponding EDS maps obtained from O Kα, Cr Kα, Co Kα, and W Lα
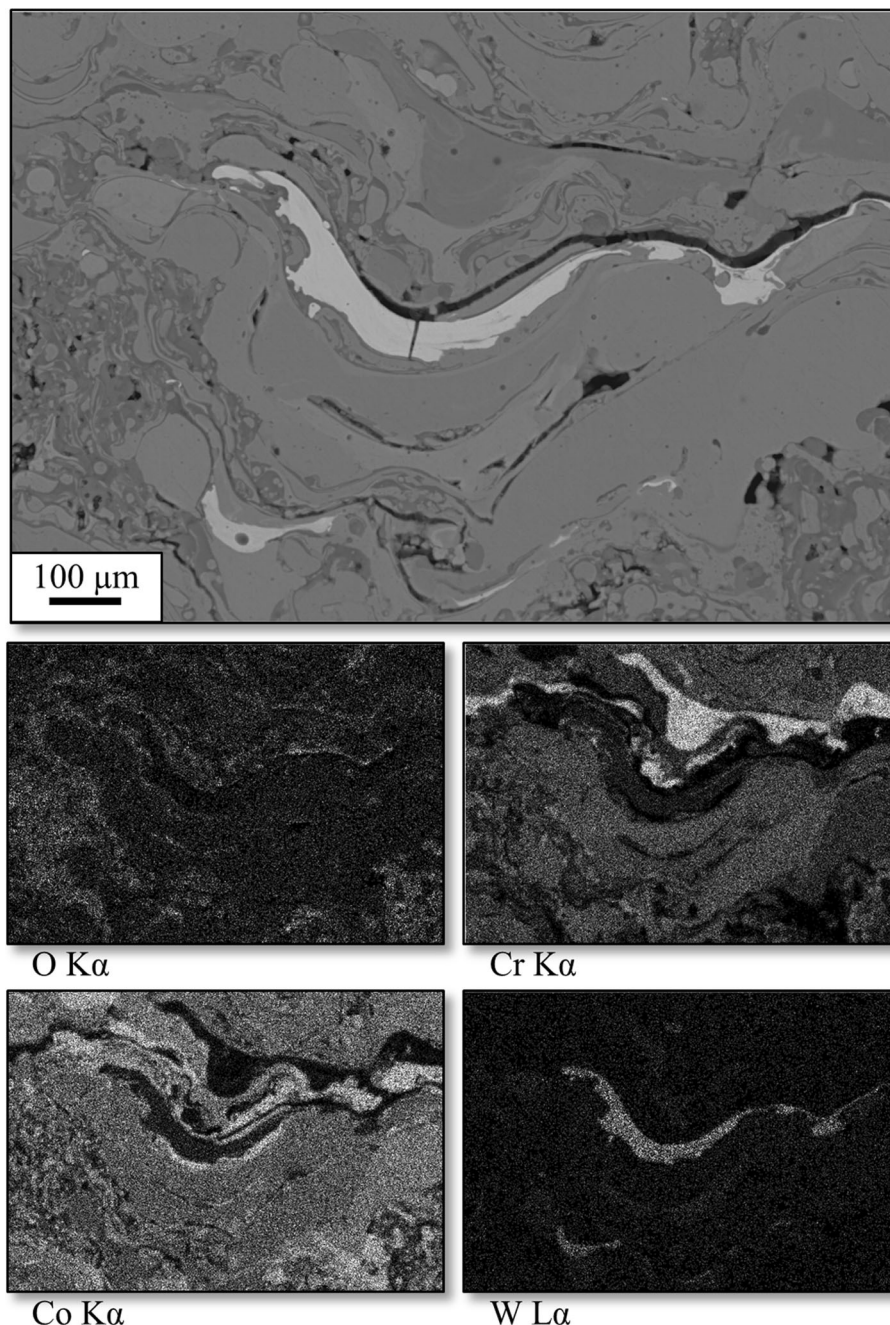

well as $NiCr_2O_4$. Due to the overlap of the Bragg reflections of $NiFe_2O_4$ and $NiCr_2O_4$ with the positions of $CoCr_2O_4$, the presence of NiFe2O4 and NiCr2O4 cannot be confirmed or completely ruled out based on the diffractograms. However, it is stated that the formation of spinel ferrites such as $NiFe_2O_4$ (or $Ni_{1.43}Fe_{1.7}O_4$) is unlikely due to the small proportion of Ni and Fe contained in the feedstock. With rising temperature, additional Bragg reflections show the formation of new phases. Above 550 °C, the XRD pattern reveals that the surface additionally consists of Fe_2O_3. With further increase in temperature, surface oxidation is amplified. Here, the

formation of Fe_2O_3 and Co_3O_4 is more pronounced, especially at a temperature of 750 °C.

Tribo-Mechanical Properties

The SI data (SI, Fig. S1) show the cross-sectional microstructure of the arc-sprayed CoCr-based coating, i.e. sample AS-S6, as well as the references HVOF-S6 and PTA-S6 which have been subjected to the dry sliding experiments. Evaluating the results obtained from the dry sliding experiments, the arc-sprayed CoCr-based coating (sample AS-S6) demonstrates a wear coefficient k of
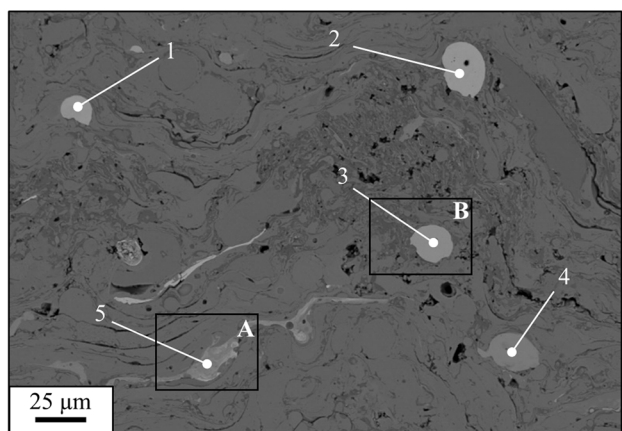
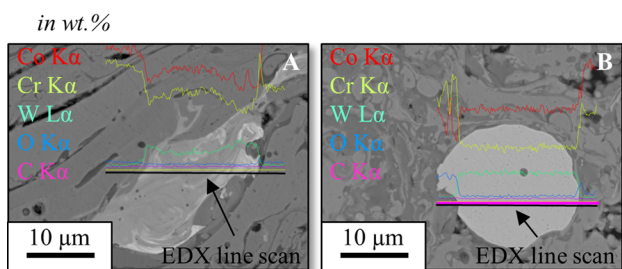| EDX spot analysis	Cr	Fe	Co	W
Spectrum 1	13.83	1.60	24.08	60.49
Spectrum 2	14.96	1.61	22.79	60.64
Spectrum 3	12.83	2.25	35.59	49.33
Spectrum 4	24.29	2.66	42.45	30.60
Spectrum 5	21.61	2.92	46.11	29.36

in wt.%

Fig. 4 SEM image showing the coating microstructure and EDS line scans at individual W-rich phases embedded in the surrounding matrix

$10.38 \pm 1.26 \cdot 10^{-5}$ mm^3 Nm (Table 1). In contrast, the samples HVOF-S6 and PTA-S6 show a k of $6.80 \pm 0.29 \cdot 10^{-5}$ and $1.41 \pm 0.37 \cdot 10^{-5}$ mm^3 Nm^{-1}, suggesting a reduced wear resistance of the arc-sprayed CoCr-based coating compared with the HVOF-sprayed Stellite^{TM} coating or weld overlay processed by PTA.

With regard to the tribological stressed surface of sample AS-S6, the SE imaging demonstrates a small amount of pits inside the wear track (Fig. 7). Fracture surface morphologies inside the pits suggest the presence of particle breakouts. Furthermore, the surface exhibits some shallow grooves (i.e. minor groove pattern) which are aligned in the direction of sliding. The BSE imaging suggests the formation of oxides in the area of pits, i.e. particle breakouts, which can be confirmed by EDS analysis. The EDS analysis also point out the absence of Al at the worn surface, indicating that no debris of alumina adhered on the tribological stressed CoCr-based coating surface. With regard to the alumina counterbody, it is found that a small amount of material adheres to the wear flat. Moreover, no discernable damage such as surface deformations, grooves

or furrows are observed. Supposed surface asperities can be attributed to material adhesion. Hence, adhesion acts as main wear mechanism. Nevertheless, severe adhesive wear on the wear flat is prevented. It is assumed that torn out wear particles (i.e. originating from the tribological stressed CoCr-based coating surface) get in between the two sliding surfaces, thus, removing a certain amount of the adherent material at the wear flat of the alumina counterbody. Simultaneously, the wear particles plough through the CoCr-based coating and cause abrasion due to three-body wear.

In terms of the references (Fig. 7), the samples PTA-S6 and HVOF-S6 show some minor grooves which are orientated in the direction of sliding. With regard to sample PTA-S6, some surface morphologies at the tribological stressed surface appear as tongue-shaped structures, suggesting material smearing and plastic deformation. With respect to sample HVOF-S6, the surface morphologies indicate the tearing out of material. Simultaneously, some flake-likes structures which can be assigned to miscellaneous oxides were noted at the wear track. Nevertheless, both references demonstrate the absence of distinct particle breakouts. Furthermore, neither cracks nor large detachments could be observed. With regard to the worn surface morphologies, no traces of Al derived from the alumina counterbody were detected by EDS.

Figure 8 shows the XRD pattern obtained for the sample AS-S6 and the references HVOF-S6 and PTA-S6. It is noticeable that the two samples AS-S6 and HVOF-S6 each consist of phase mixtures, whereas the cubic Co phase is dominant in sample PTA-S6. The sample AS-S6 shows a mixture of cubic and hexagonal Co, cubic Cr and CoCr$_2$, while the sample HVOF-S6 is composed of a mixture of cubic Cr and Co. It is known that the formation of CoCr solid solutions (Ref 53) and strain-induced Co-fcc to Co-hcp phase transformations (Ref 54, 55) could cause an increased surface hardness. Thus, higher hardness values are expected for the AS-S6 and HVOF-S6 samples compared to the PTA-S6 sample which will be discussed in the next paragraph.

To evaluate the mechanical response at the contact area of the tribological stressed surface, hardness measurements (i.e. nanoindentation, Vickers indentation) were conducted inside the wear track and compared to the results obtained from the non-tribological stressed coating surface (Table 1). For sample AS-S6, a hardness of 6.7 ± 1.7 GPa was measured inside the wear track, whereas the non-tribological stressed coating surface exhibits a hardness of 5.5 ± 0.8 GPa. Vickers microhardness measurement confirms the increase in hardness at the wear track. Hence, the worn coating surface demonstrates a Vickers microhardness of 515 ± 44 HV0.3, while the non-tribological stressed surface shows a Vickers microhardness of

Fig. 5 XRD pattern of the arc-sprayed CoCr-based coating, and the cored wire used for depositing coating (i.e. filling and velum)
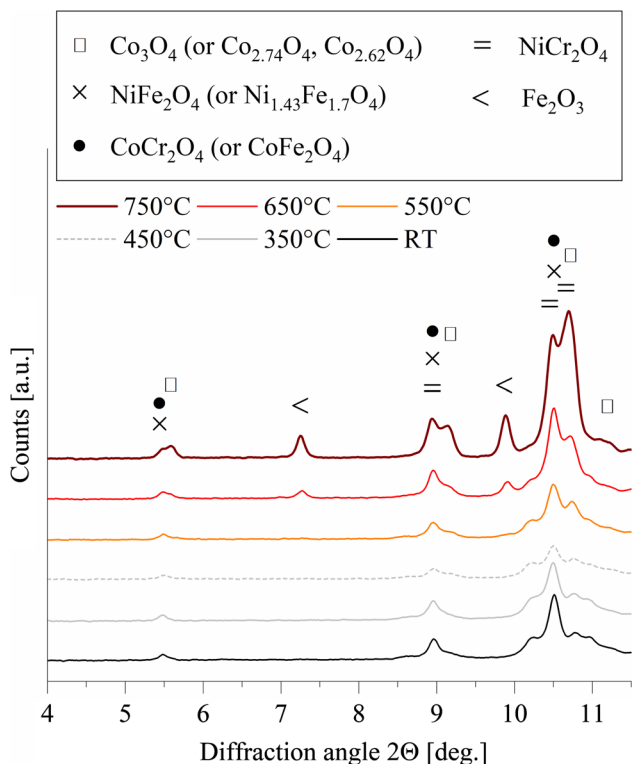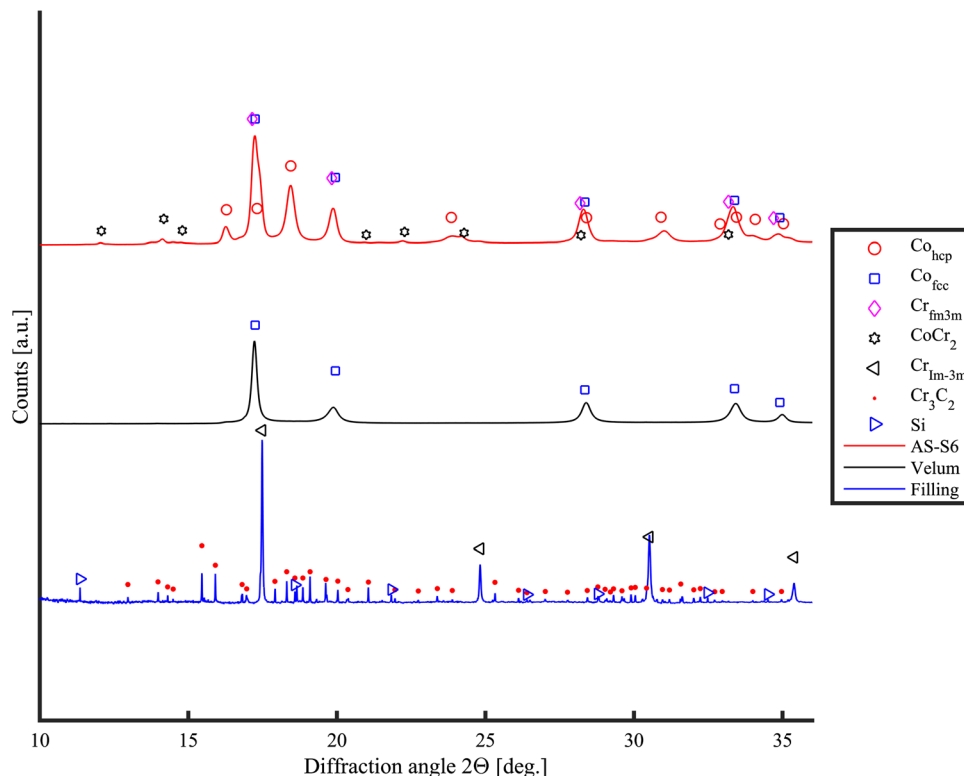

Fig. 6 XRD pattern of the coating surface at room temperature (RT) as well as after exposure to elevated temperatures (i.e. 350, 450, 550, 650, and 750 °C)

498 ± 50 HV0.3. Similar tendencies are noted for the references HVOF-S6 and PTA-S6. Compared to the non-tribological stressed surface, an increase in hardness and Vickers microhardness is measured inside the wear track for sample HVOF-S6 and PTA-S6. In comparison with sample AS-S6, however, the increase in hardness and Vickers microhardness inside the wear track for both references is more pronounced. Nanoindentation experiments additionally reveal a H/E and H^3/E^2 ratio of 0.049 and 0.017 (versus H/E = 0.046 and H^3/E^2 = 0.012 at the non-tribological stressed coating surface) for the tribological stressed surface of sample AS-S6, whereas the reference HVOF-S6 exhibits a H/E and H^3/E^2 ratio of 0.050 and 0.022 (versus H/E = 0.043 and H^3/E^2 = 0.012 at the non-tribological stressed coating surface). As opposed to that, the reference PTA-S6 demonstrates a H/E and H^3/E^2 ratio of 0.035 and 0.010 (versus H/E = 0.021 and H^3/E^2 = 0.002 at the non-tribological stressed coating surface), which corresponds to the lowest values calculated within the measurements. The resistance to plastic deformation, the H^3/E^2 ratio, is a significant factor determining the wear resistance against sliding. Typically, the higher the H^3/E^2 ratio, the higher the resistance to plastic deformation. The values for the H^3/E^2 or H/E ratio determined here do not agree with the observations in the dry sliding experiments, i.e. the calculated wear coefficients. In particular, the

Table 1 Mechanical properties of selected CoCr-based coatings produced by different processes

	Samples		
	AS-S6	HVOF-S6	PTA-S6
Vickers indentation			
Microhardness (polished surface), HV0.3	498 ± 50	550 ± 45	303 ± 20
Microhardness (wear track), HV0.3	515 ± 44	679 ± 17	578 ± 80
Fracture toughness, K_{IC}, MPa m$^{1/2}$	1.30 ± 0.59	1.55 ± 0.18	n.m.[a]
Nanoindentation			
Hardness (polished surface), GPa	5.5 ± 0.7	6.8 ± 1.2	4.9 ± 0.3
Hardness (wear track), GPa	6.8 ± 1.7	9.0 ± 1.3	7.8 ± 1.4
Young's modulus (polished surface), GPa	120 ± 14	160 ± 24	232 ± 6
Young's modulus (wear track), GPa	138 ± 24	181 ± 19	223 ± 26
Dry sliding experiments			
Wear coefficient k, $10^{-5} \cdot$ mm^3 Nm^{-1}	10.38 ± 1.26	6.80 ± 0.29	1.41 ± 0.37
Coefficient of friction	0.49 ± 0.01	0.48 ± 0.01	0.57 ± 0.02

[a]*not measurable by means of Vickers indentation*

reference PTA-S6 demonstrated an enhanced wear resistance against sliding, as shown by a reduced wear coefficient compared to sample AS-S6, despite a lower H^3/E^2 or H/E ratio. In general, the load and displacement sensing indentation represents an attractive technique for extracting Young's moduli. Nevertheless, for a heterogeneous coating microstructure, the measurement is problematic and may be affected by the coating's porosity and oxidation phenomena. It is known, for example, that the Young's modulus of porous samples decreases with increasing porosity. As a result, the Young's modulus of each sample (i.e. AS-S6, HVOF-S6 and PTA-S6) largely depends on the porosity degree. It can be concluded that for the tested samples, the wear resistance against sliding cannot be explained solely by the hardness, Vickers microhardness, as well as the H^3/E^2 or H/E ratio.

With respect to the fracture toughness measurements, the Vickers indentation reveals that the sample AS-S6 possesses a fracture toughness K_{IC} of 1.30 ± 0.59 MPa m$^{1/2}$. The HVOF-sprayed reference, i.e. sample HVOF-S6, shows a fracture toughness K_{IC} of 1.55 ± 0.18 MPa m$^{1/2}$. In contrast, the fracture toughness K_{IC} for sample PTA-S6 could not be measured. Although serval indents were placed, crack initiation could not be observed, suggesting a higher fracture toughness K_{IC} for sample PTA-S6.

It is striking that the fracture toughness K_{IC} for sample AS-S6 and HVOF-S6 is remarkable low compared with those observed for Stellite™ hardfacing alloys (Ref 56). Several constraints need to be taken into account to get reliable results (i.e. the formation of cracks originated from the corner of Vickers indents, mechanism of cracks spreading or propagating through the coating). Houdková et al. (Ref 57) critically discussed the validity of such indentation fracture toughness models for HVOF-sprayed Co-based coatings such as Stellite™. The authors therefore claimed that the postulated model to determine the fracture toughness is not valid for the arc-sprayed and HVOF-sprayed CoCr-based coatings. Nevertheless, the tendency that the arc-sprayed CoCr-based coating provides a reduced hardness and fracture toughness K_{IC} compared to the references (in particular to the CoCr-based reference processed by PTA) is likely to result in a decreased wear resistance against sliding. Due to the inherent process characteristics, i.e. spraying at ambient conditions, the arc-sprayed CoCr-based coating is interstratified with various oxides. Phase transformation processes, including those such as oxide formation, imply a limited ductility of the coating material. Due to the cycling movement of the alumina ball over the coating surface during dry sliding, the coating surface is subjected to Hertzian contact stress. Thus, the material suffers from the mechanical cycling loads, which results in crack initiation. If the load is particularly severe, the cracks further propagate which in turn favours the emergence of particle breakouts. Accordingly, it is stated that the particle breakouts (Fig. 7) result from surface fatigue driven by Hertzian contact stress. The importance of fracture toughness K_{IC} in this case is substantiated by the fact that the CoCr-based reference processed by PTA exhibits a higher wear resistance against sliding compared to the HVOF-sprayed CoCr-based coating, despite the latter demonstrates an increased hardness.

Evaluating the coefficient of friction (COF) during the dry sliding experiments, the tribological stressed surfaces demonstrate a running-in behaviour in the beginning of the tribological test which has stabilized after approximately 50 m (samples AS-S6 and PTA-S6), respectively, after almost 75 m (sample HVOF-S6), and remains nearly constant with increasing sliding distance (as shown for
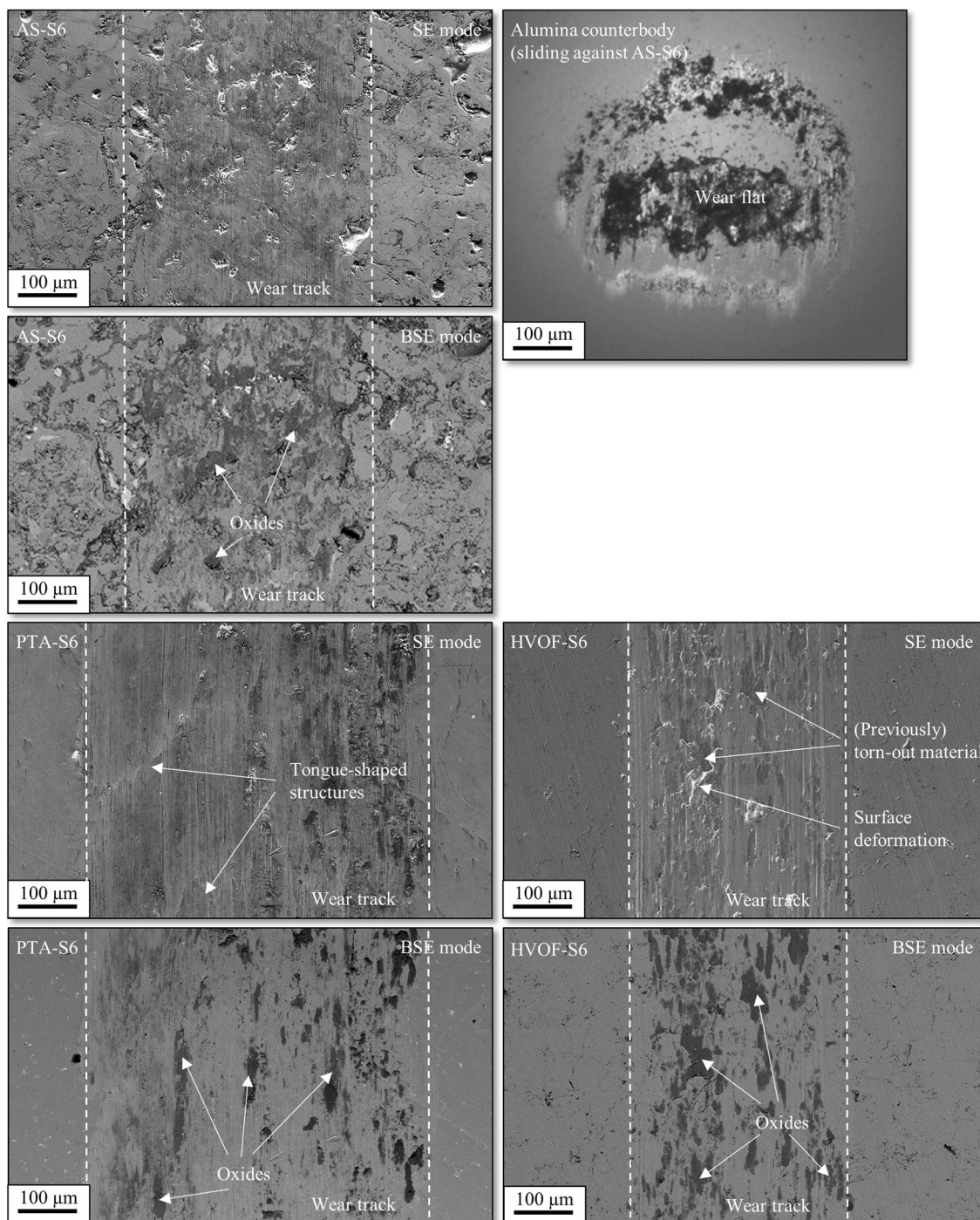
Fig. 7 SEM images showing the wear track at the tribological stressed surface of the arc-sprayed CoCr-based coating after sliding against the alumina counterbody, as well as the corresponding wear flat of the alumina counterbody taken by light microscopy. The tribologically stressed surfaces of the CoCr-based reference samples are attached

representative samples in Fig. 9). Comparing the running-in behaviour of the different samples with each other it can be noticed that the samples PTA-S6 and HVOF-S6 show an erratic COF. In contrast, the sample AS-S6 demonstrates a completely different running-in behaviour. In this case, a steady increase of the COF can be observed before it becomes almost constant with increasing sliding distance. In the steady state, the sample AS-S6 exhibits a mean

Fig. 8 XRD pattern of the arc-sprayed CoCr-based coating and CoCr-based reference samples
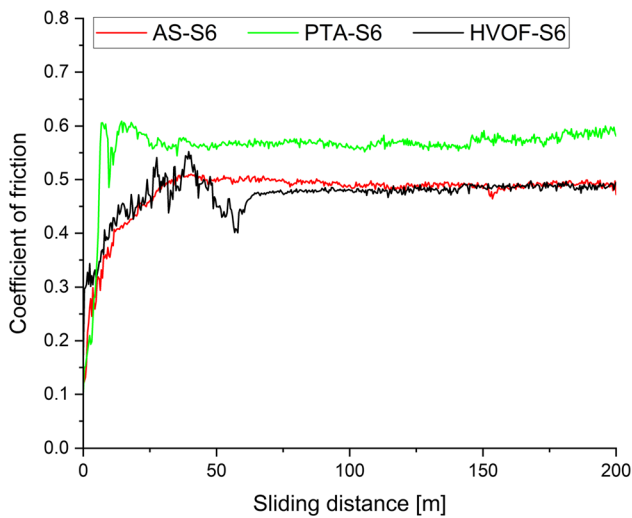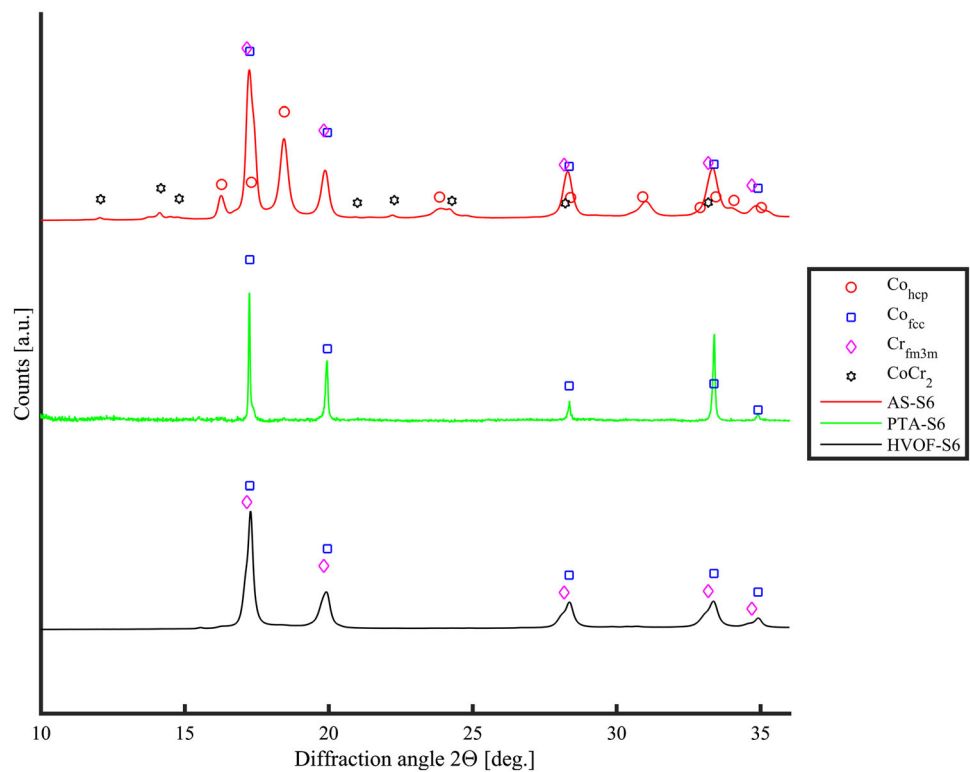

Fig. 9 Evolution of the COF of selected measurements representing the arc-sprayed CoCr-based coating and the CoCr-based reference samples

COF_{AS-S6} of 0.49 ± 0.01, whereas the references HVOF-S6 and PTA-S6 reveal a mean $COF_{HVOF-S6}$ of 0.48 ± 0.01, and a mean COF_{PTA-S6} of 0.57 ± 0.02, respectively, sliding against alumina. In general, however, no significant fluctuations of the COF can be observed within increasing sliding distance for the investigated samples. The findings

within this study indicate that the COF of the arc-sprayed CoCr-based coating is found to be similar to the COF obtained for the HVOF-sprayed CoCr-based coating, but lower than the COF of the CoCr-based hardfacing alloy deposited by PTA. The authors assume that the friction behaviour of the arc-sprayed CoCr-based coating is predominantly determined by the presence of metal oxides (randomly interstratified in the coating due to spraying under ambient conditions or discrete at particle breakouts) at the contact area between the two sliding surfaces. With regard to the CoCr-based reference samples, tribo-oxidation phenomena favour a similar friction behaviour. Besides the formation of oxides, however, the references also exhibit a small amount of material smearing and plastic deformation. Accordingly, the slightly increased COF, as found for the CoCr-based hardfacing alloy deposited by PTA, is likely attributed to material smearing and surface deformation. Since the arc-sprayed CoCr-based coating shows, almost exclusively, the emergence of particle breakouts resulting from surface fatigue, the authors assume that the improved COF is at the expense of service life. In future tribological investigations, the long-term behaviour under dry sliding conditions should therefore be analysed.

Conclusion

This study aimed at evaluating the microstructural and tribo-mechanical properties of an arc-sprayed CoCr-based coating. The findings of tribological testing were compared to those obtained from conventional CoCr-based coatings processed by HVOF and PTA.

As verified by electron microscopy and EDS, the arc-sprayed CoCr-based coating consists of a heterogeneous microstructure which is mainly composed of Co-rich, Cr-rich lamellae or lamellae comprising a Co(Cr)-rich solid solution. In addition, miscellaneous oxides were formed and embedded between individual lamellae. A certain amount of W-rich particles could be found which scattered randomly across the coating. Local spot analyses revealed the absence of tungsten carbides within the experimental resolution (i.e. EDS, or XRD). Instead, EDS analysis suggests that the W-rich particles consist of a W(Co, Cr) solid solution with a higher amount of Co. With respect to the oxidation behaviour, the as-sprayed coating predominantly contains $CoCr_2O_4$ as well as traces Co_3O_4. At high temperatures above 550 °C, the coating surface shows the formation of Fe_2O_3 and Co_3O_4, with Co_3O_4 being more pronounced at a temperature of 750 °C. It is assumed that the microstructural heterogeneity can be attributed to the cored wire configuration used within this study as well as the electrode phenomena during atomization, i.e. when W-rich particles are partially or completely molten and wetted by the molten metal such as the wire sheath (Co phase), or filler material (Cr phase). The findings rather suggest that solid solution hardening serves as dominant strengthening mechanism, while precipitation hardening effects such as the formation of carbides are hardly evident. Dry sliding experiments demonstrated that the arc-sprayed CoCr-based coating exhibits a reduced wear resistance compared to CoCr-based coatings processed by HVOF and PTA. Since the arc-sprayed CoCr-based coating was prone to show a higher amount of particle breakouts at the tribological stressed surface, the wear behaviour differs from the one found for the CoCr-based coatings deposited by HVOF and PTA. Moreover, the arc-sprayed CoCr-based coatings demonstrated a good friction behaviour with a COF of approximately 0.5 similar to the COF obtained for the HVOF-sprayed CoCr-based coating, but lower than the COF of the CoCr-based hardfacing alloy deposited by PTA.

References

1. H.E. Exner, Physical and Chemical Nature of Cemented Carbides, *Int. Met. Revi.*, 1979, **24**(1), p 149-173.

2. P.D. Wood, H.E. Evans, and C.B. Ponton, Investigation into the Wear Behaviour of Stellite 6 During Rotation as an Unlubricated Bearing at 600°C, *Tribol. Int.*, 2011, **44**(12), p 1589-1597.

3. M.M. Ferozkhan, M. Duraiselvam and K.G. kumar, and R. Ravibharath, Plasma Transferred Arc Welding of Stellite 6 Alloy on Stainless Steel for Wear Resistance, *Procedia Technology*, 2016, **25**, p 1305-1311.

4. G.R. Mirshekari, S. Daee, S.F. Bonabi, M.R. Tavakoli, A. Shafyei, and M. Safaei, Effect of Interlayers on the Microstructure and Wear Resistance of Stellite 6 Coatings Deposited on AISI 420 Stainless Steel by GTAW Technique, *Surf. Interfaces*, 2017, **9**, p 79-92.

5. J.-C. Shin, J.-M. Doh, J.-K. Yoon, D.-Y. Lee, and J.-S. Kim, Effect of Molybdenum on the Microstructure and Wear Resistance of Cobalt-Base Stellite Hardfacing Alloys, *Surf. Coat. Technol.*, 2003, **166**(2-3), p 117-126.

6. P. Sassatelli, G. Bolelli, M. Lassinantti Gualtieri, E. Heinonen, M. Honkanen, L. Lusvarghi, T. Manfredini, R. Rigon, and M. Vippola, Properties of HVOF-Sprayed Stellite-6 Coatings, *Surf. Coat. Technol.*, 2018, **338**, p 45-62.

7. T.S. Sidhu, S. Prakash, and R.D. Agrawal, Studies of the Metallurgical and Mechanical Properties of High Velocity Oxy-Fuel Sprayed Stellite-6 Coatings on Ni- and Fe-Based Superalloys, *Surf. Coat. Technol.*, 2006, **201**(1-2), p 273-281.

8. A. Kusmoko, D. Dunne, and H. Li, A Comparative Study for Wear Resistant of Stellite 6 Coatings on Nickel Alloy Substrate Produced By Laser Cladding, *HVOF and Plasma Spray. Tech. IJSER*, 2014, **4**, p 32-36.

9. N. Jegadeeswaran, K. Udaya Bhat, and M.R. Ramesh, Oxidation Studies on As-Received and HVOF Sprayed Stellite-6 Coating on Turbine Alloys at 800 °C, *IJSER*, 2013, **4**, p 214-220.

10. Š Houdková, Z. Pala, E. Smazalová, M. Vostřák, and Z. Česánek, Microstructure and Sliding Wear Properties of HVOF Sprayed, Laser Remelted and Laser Clad Stellite 6 Coatings, *Surf. Coat. Technol.*, 2017, **318**, p 129-141.

11. R. Singh, D. Kumar, S.K. Mishra, and S.K. Tiwari, Laser Cladding of Stellite 6 on Stainless Steel to Enhance Solid Particle Erosion and Cavitation Resistance, *Surf. Coat. Technol.*, 2014, **251**, p 87-97.

12. M.S. Sawant and N.K. Jain, Evaluation of Stellite Coatings by μ-PTA Powder, Laser, and PTA Deposition Processes, *Mater. Manuf. Processes*, 2018, **33**(10), p 1043-1050.

13. H. Kashani, A. Amadeh, and H.M. Ghasemi, Room and High Temperature Wear Behaviors of Nickel and Cobalt Base Weld Overlay Coatings on Hot Forging Dies, *Wear*, 2007, **262**(7-8), p 800-806.

14. H. Zhang, Y. Gong, X. Chen, A. McDonald, and H. Li, A Comparative Study of Cavitation Erosion Resistance of Several HVOF-Sprayed Coatings in Deionized Water and Artificial Seawater, *J. Therm. Spray Technol.*, 2019, **28**(5), p 1060-1071.

15. A. Kumar, J. Boy, R. Zatorski, and L.D. Stephenson, Thermal Spray and Weld Repair Alloys for the Repair of Cavitation Damage in Turbines and Pumps: A Technical Note, *J. Therm. Spray Technol.*, 2005, **14**(2), p 177-182.

16. H.S. Sidhu, B.S. Sidhu, and S. Prakash, Hot Corrosion Behavior of HVOF Sprayed Coatings on ASTM SA213-T11 Steel, *J. Therm. Spray Technol.*, 2007, **16**(3), p 349-354.

17. A.S. Kang, J.S. Grewal, and G.S. Cheema, Effect of Thermal Spray Coatings on Wear Behavior of High Tensile Steel Applicable for Tiller Blades, *Mater. Today: Proc.*, 2017, **4**(2), p 95-103.

18. DHE Persson, On the Mechanisms Behind the Tribological Performance of Stellites, Uppsala University, doctoral thesis, 2005

19. T.W. Scharf, S.V. Prasad, P.G. Kotula, J.R. Michael, and C.V. Robino, Elevated Temperature Tribology of Cobalt and Tantalum-Based Alloys, *Wear*, 2015, **330–331**, p 199-208.

20. D.H.E. Persson, S. Jacobson, and S. Hogmark, The Influence of Phase Transformations and Oxidation on the Galling Resistance and Low Friction Behaviour of a Laser Processed Co-Based Alloy, *Wear*, 2003, **254**(11), p 1134-1140.

21. Y. Birol, High Temperature Sliding Wear Behaviour of Inconel 617 and Stellite 6 alloys, *Wear*, 2010, **269**(9-10), p 664-671.

22. A. Motallebzadeh, E. Atar, and H. Cimenoglu, Raman Spectroscopy Characterization of Hypo-Eutectic CoCrWC Alloy Tribolayers, *Ind. Lubr. Tribol.*, 2016, **68**(4), p 515-520.

23. L. da Conceição and A.S.C.M. D'Oliveira, The Effect of Oxidation on the Tribolayer and Sliding Wear of a Co-Based Coating, *Surf. Coat. Technol.*, 2016, **288**, p 69-78.

24. DURUM Verschleißschutz, Produkte, Fülldrähte. https://durmat.com/produkte/fuelldraehte/#kobalt-basis.

25. Deloro, Product Information, Hardfacing Alloys. https://www.deloro.com/productinformation/.

26. R. Varavallo, M.D. Manfrinato, L.S. Rossino, O. Maluf, and F. Camargo, Adhesion of Thermally Sprayed Metallic Coating, 18Th International Federation For Heat Treatment and Surface Engineering: International Federation for Heat Treatment and Surface Engineering congress, held in Rio de Janeiro, Brazil, July 26 - 30, 2010, L.d.C.F. Canale, Ed., ASTM Internat, 2012, p 559-573.

27. B. Wielage, H. Pokhmurska, M. Student, V. Gvozdeckii, T. Stupnyckyj, and V. Pokhmurskii, Iron-Based Coatings Arc-Sprayed with Cored Wires for Applications at Elevated Temperatures, *Surf. Coat. Technol.*, 2013, **220**, p 27–35.

28. Amir Hossein Pourmousa Abkenar, Wire-arc spraying system: Particle production, transport, and deposition, Library and Archives Canada = Bibliothèque et Archives Canada, 2007.

29. H.J. Fahrenwaldt and V. Schuler, Praxiswissen Schweißtechnik, Springer, 2012 (in ger).

30. A. Pourmousa, J. Mostaghimi, A. Abedini, and S. Chandra, Particle Size Distribution in a Wire-Arc Spraying System, *J. Therm. Spray. Tech.*, 2005, **14**(4), p 502-510.

31. M.P. Planche, H. Liao, and C. Coddet, Relationships between In-Flight Particle Characteristics and Coating Microstructure with a Twin Wire Arc Spray Process and Different Working Conditions, *Surf. Coat. Technol.*, 2004, **182**(2-3), p 215-226.

32. A.P. Newbery, P.S. Grant, and R.A. Neiser, The Velocity and Temperature of Steel Droplets during Electric Arc Spraying, *Surf. Coat. Technol.*, 2005, **195**(1), p 91-101.

33. H.L. Liao, Y.L. Zhu, R. Bolot, C. Coddet, and S.N. Ma, Size Distribution of Particles from Individual Wires and the Effects of Nozzle Geometry in Twin Wire Arc Spraying, *Surf. Coat. Technol.*, 2005, **200**(7), p 2123-2130.

34. N.A. Hussary and J.V.R. Heberlein, Effect of System Parameters on Metal Breakup and Particle Formation in the Wire Arc Spray Process, *J. Therm. Spray. Tech.*, 2007, **16**(1), p 140-152.

35. M. Kelkar and J. Heberlein, Wire-Arc Spray Modeling, *Plasma Chem. Plasma Process.*, 2002, **22**(1), p 1-25.

36. N.A. Hussary and J.V.R. Heberlein, Atomization and Particle-Jet Interactions in the Wire-Arc Spraying Process, *J Therm Spray Tech*, 2001, **10**(4), p 604-610.

37. JJ Fang, ZX Li, M Qian, CL Ren, and YW Shi, Effects of Powder Size in Cored Wire on Arc-Sprayed Metal-Ceramic Coatings, *Global Coating Solutions: Proceedings of the 2007 International Thermal Spray Conference*, May 14-16, 2007, Beijing, People's Republic of China, B.R. Marple, Ed., ASM International, 2007, p 365-370.

38. V. Boronenkov and Y. Korobov, Fundamentals of Arc Spraying, Springer International Publishing, 2016.

39. G. Jandin, H. Liao, Z.Q. Feng, and C. Coddet, Correlations between Operating Conditions, Microstructure and Mechanical Properties of Twin Wire Arc Sprayed Steel Coatings, *Mater. Sci. Eng., A*, 2003, **349**(1-2), p 298-305.

40. I. Gedzevicius and A.V. Valiulis, Analysis of Wire Arc Spraying Process Variables on Coatings Properties, *J. Mater. Process. Technol.*, 2006, **175**(1-3), p 206-211.

41. P. Niranatlumpong and H. Koiprasert, Phase Transformation of NiCrBSi–WC and NiBSi–WC Arc Sprayed Coatings, *Surf. Coat. Technol.*, 2011, **206**(2-3), p 440-445.

42. W. Tillmann and M. Abdulgader, Wire Composition: Its Effect on Metal Disintegration and Particle Formation in Twin-Wire Arc-Spraying Process, *J Therm Spray Tech*, 2013, **22**(2-3), p 352-362.

43. A.P. Newbery and P.S. Grant, Oxidation During Electric Arc Spray Forming of Steel, *J. Mater. Process. Technol.*, 2006, **178**(1-3), p 259-269.

44. G. Derringer and R. Suich, Simultaneous Optimization of Several Response Variables, *J. Qual. Technol.*, 1980, **12**, p 214-219.

45. W. Tillmann, L. Hagen, and D. Duda, A Study on the Tribological Behavior of Arc Sprayed Vanadium doped Stellite Coatings, *Thermal Spray 2017: Proceedings from the International Thermal Spray Conference,* June 7-9, 2017, Düsseldorf, Germany, 2017, DVS 336, p 354-359.

46. C. Krywka, M. Paulus, C. Sternemann, M. Volmer, A. Remhof, G. Nowak, A. Nefedov, B. Pöter, M. Spiegel, and M. Tolan, The New Diffractometer for Surface X-ray Diffraction at Beamline BL9 of DELTA, *J. Synchrotron Radiat.*, 2006, **13**, p 8-13.

47. W.C. Oliver and G.M. Pharr, An Improved Technique for Determining Hardness and Elastic Modulus Using Load and Displacement Sensing Indentation Experiments, *J. Mater. Res.*, 1992, **7**(6), p 1564-1583.

48. J.B. Cheng, X.B. Liang, and B.S. Xu, Devitrification of Arc-Sprayed FeBSiNb Amorphous Coatings: Effects on Wear Resistance and Mechanical Behavior, *Surf. Coat. Technol.*, 2013, **235**, p 720-726.

49. F. Cai, X. Huang, and Q. Yang, Mechanical Properties, Sliding Wear and Solid Particle Erosion Behaviors of Plasma Enhanced

Magnetron Sputtering CrSiCN Coating Systems, *Wear*, 2015, **324–325**, p 27-35.

50. J. Musil, F. Kunc, H. Zeman, and H. Poláková, Relationships between hardness, Young's modulus and Elastic Recovery in Hard Nanocomposite Coatings, *Surf. Coat. Technol.*, 2002, **154**(2-3), p 304-313.

51. D.K. Shetty and I.G. Wright, On Estimating Fracture Toughness of Cemented Carbides from Palmqvist Crack Sizes, Journal of Materials Science Letters, 3rd ed., Chapman & Hall, Ed., 1986, p 365-368.

52. K. Niihara, A 1983 Fracture Mechanics Analysis of Indentation-Induced Palmqvist Crack in Ceramics, *J. mater. Sci. let.*, 1983, **2**(5), p 221-223.

53. E. Cabrol, C. Boher, V. Vidal, F. Rezai-Aria, and F. Touratier, Plastic Strain of Cobalt-Based Hardfacings Under Friction Loading, *Wear*, 2015, **330-331**, p 354-363.

54. H. Kashani, M. Sadeghi Laridjani, A. Amadeh, M. Khodagholi, and S. Ahmadzadeh, The Influence of Volumetric Dilution on the Strain Induced $\gamma \rightarrow \varepsilon$ Martensitic Transformation in GTAW Processed Co–Cr–Mo alloy, *Mater. Sci. Eng. A*, 2008, **478**, p 38-42.

55. M. Yildirim and A. Keles, Effect of Aging Time on Phase Transformation, Microstructure and Hardness of Co-Cr-Mo Alloys, *Selcuk Univ. J. Eng. Sci. Tech.*, 2019, **7**(1), p 146-153.

56. B.V. Cockeram, Fracture Toughness Testing and Toughening Mechanisms of Some Commercial Cobalt-Free Hardfacing Alloys, *Surf. Coat. Technol.*, 1998, **108-109**, p 377-384.

57. Š Houdková, E. Smazalová, and Z. Pala, Effect of Heat Treatment on the Microstructure and Properties of HVOF-Sprayed Co-Cr-W Coating, *J Therm Spray Tech*, 2016, **25**(3), p 546-557.